Supercritical Angle Fluorescence Microscopy and Spectroscopy

Martin Oheim, Adi Salomon, Maia Brunstein

Biophysical Review

Supercritical angle fluorescence microscopy and spectroscopy

Running title: Fluorescence imaging from forbidden angles

Martin Oheim,[*,a,✉] Adi Salomon,[*,†,b] and Maia Brunstein,[*,‡]

*Université de Paris, SPPIN - Saints-Pères Paris Institute for the Neurosciences, CNRS, Paris F-75006, France;
†Institute of Nanotechnology and Advanced Materials (BINA), Department of Chemistry, Bar-Ilan University, Ramat-Gan, 52900 Israel;
‡Chaire d'Excellence Junior, Université Sorbonne Paris Cité, Paris, F-75006 France.

Address all correspondence to

✉ martin.oheim@parisdescartes.fr

SPPIN - Saints-Pères Paris Institute for the Neurosciences
Centre National de la Recherche Scientifique, CNRS UMR 8003
Université de Paris, Campus Saint-Germain-des-Prés
45 rue des Saints Pères
F-75006 Paris, France

Phone: +33 1 42 86 42 21 (lab), -42 22 (office)

[a)] MO was a *Joseph Meyerhof Invited Professor* with the Department of Biomolecular Sciences, The Weizmann Institute for Science, Rehovot, Israel, during the academic year 2018-19.

[b)] Adi Salomon is currently a *Chateaubriand Senior Research Fellow* with the SPPIN.

ABSTRACT. Fluorescence detection, either involving propagating or near-field emission, is widely being used in spectroscopy, sensing and microscopy. Total internal reflection fluorescence (TIRF) confines fluorescence excitation by an evanescent (near-) field and it is a popular contrast generator for surface-selective fluorescence assays. Its emission equivalent, supercritical angle fluorescence (SAF) is comparably less established although it achieves a similar optical sectioning as does TIRF. SAF emerges when a fluorescing molecule is located very close to an interface and its near-field emission couples to the higher-refractive index medium ($n_2 > n_1$) and becomes propagative. Then, most fluorescence is detectable on the side of the higher-index substrate and a large fraction of this fluorescence is emitted into angles forbidden by Snell's law. SAF as well as the undercritical angle fluorescence (UAF, far-field emission) components can be collected with microscope objectives having a high-enough detection aperture (NA > n_2) and be separated in the back-focal plane (BFP) by Fourier filtering. The BFP image encodes information about the fluorophore radiation pattern, and it can be analysed to yield precise information about the refractive index in which the emitters are embedded, their nanometric distance from the interface and their orientation. A SAF microscope can retrieve this near-field information through wide-field optics in a spatially resolved manner, and this functionality can be added to an existing inverted microscope. Here, we describe the potential underpinning of SAF microscopy and spectroscopy, particularly in comparison with TIRF. We review the challenges and opportunities that SAF presents from a biophysical perspective, and we discuss areas where we see potential.
[220 words]

Significance statement

Many processes happen close to or at an interface. Battery electrodes, biofilm growth, transport and signaling across cellular membranes, or phase mixing are just a few examples of such phenomena. While fluorescence-based detection techniques are standard, their surface-selective variants require the elimination of bulk background fluorescence to detect near-interface molecules in isolation. Near-field techniques usually require specialized instrumentations but there is an optical phenomenon called supercritical-angle fluorescence (SAF) that makes near-field information available in the far field. As SAF can originate from near-interface fluorophores only and these molecules emit a highly directional fluorescence, SAF has a unique signature that permits its separation from classical bulk fluorescence. SAF can be captured by a high-numerical aperture objective and imaged in its back-focal plane and it contains not only information about the molecule, but also about its environment. [997 charac.]

INTRODUCTION

SUPERCRITICAL ANGLE FLUORESCENCE [1] (SAF) designates fluorescence directed into emission angles forbidden for far-field light. Virtually unknown even among experts only a couple of years ago, SAF is increasingly being used in, fluorescence detection and spectroscopy, but also in near-surface imaging applications and in SAF-based refractometry. A growing body of super-resolution literature combines SAF for nanometer axial fluorophore localization (along the microscope's optical axis) with other techniques that improve the lateral resolution. This *Biophysical Review* provides an update on the growing field of SAF and it is organized in five sections. In the first section, we review the physics of dipole near-field emission and explain how SAF becomes detectable in the far-field. We argue that SAF can be understood as the optical reciprocal of TIRF with a similar optical section capacity. In section II, we discuss the use of SAF for imaging applications, and we also explore the (at first sight not-so-obvious) interest of combined TIRF excitation and SAF detection. In the third chapter, we shed light on the different experimental strategies to separate under- and supercritical emission components, before section IV gives an overview of recent SAF applications. In the final section V, we try to anticipate future directions of research and we give a subjective perspective on what might be next in biophysical uses of SAF.

I. SUPERCRITICAL ANGLE FLUORESCENCE, A TWIN AND COMPANION TO TIRF

"*If you can see me, I can see you*"

OPTICAL RECIPROCITY is key for understanding SAF, or "forbidden-light detection" (1). SAF has been dubbed "evanescence in emission" (2), much as TOTAL INTERNAL REFLECTION fluorescence (TIRF) refers to "evanescence in excitation". Common to either optical phenomenon are near-field interactions of light with a dielectric material. When light hits the interface, the angles of refraction and reflection are governed by SNELL'S LAW, and the transmitted and refracted intensities are given by the Fresnel coef-ficients, **Fig. 1***A* (*top*). For

[1] Terms in SMALL CAPS are explained in the Glossary at the end of this Review Article.

supercritical angles, i.e., $\theta_2 \geq \theta_c = \text{asin}(n_1/n_2)$ the reflection is total so that $I_{refl} = I_0$ and an evanescent wave (EW) is generated just above the boundary as a consequence of energy and momentum conservation. This inhomogeneous surface wave skims the optically rarer medium and it propagates along $+x$ for an incidence from the left as illustrated in panel A. The EW intensity decays exponentially with distance z from the interface with a length-constant $\delta = \lambda/[4\pi\cdot(n_2^2\cdot\sin^2(\theta)-n_1^2)^{1/2}]$. For most realistic optical interfaces δ is of the order of $\lambda/4$. Here λ denotes the wave-length of light. If a fluorophore is present at a height h above the interface, then the EW excites fluorescence in proportion to $I(h)/I_0 \sim \exp[-h/\delta(\theta)]$, **Fig. 1***A* (*bottom*). Thus, fluore-scence excitation will be confined to a thin slice of roughly 2δ thickness, as further discussed in refs. (3, 4).

Fluorescence emission has both near- and far-field components. The far-field of a radiating dipole displays the well-known 'laying-eight' angular emission pattern with an intensity maximum perpendicular to the dipole axis, **Fig. 1***B* (*top*). When the molecule rotates, (e.g., in solution) its time-averaged far-field emission will be isotropic. For a dipole located at a height $h >> \lambda$ from the dielectric interface the collected fraction of isotropically emitted fluorescence scales as $\Omega/4\pi = \Phi = ½ [1 - \cos(\theta_{NA})] = ½ [1-(1-(NA/n_2)^2)^{1/2}]$, where $\theta_{NA} = \text{asin}(NA/n_2)$. For a NA-1.45 TIRF objective, Φ is of the order of 36%, which means that only one third of the total emitted fluorescence is collected, and this despite the large NA of the TIRF objective lens.

In addition to its far-field, dipole emission has a near-field component, too (2). Dipole emission in uniform media has components that decay $\propto 1/r$, $1/r^2$ and $1/r^3$. The exponentially dwindling 'evanescent' component only exists in the presence of an interface between optical media with different indices of refraction. ($h \leq \lambda$). The emission is converted by the proximity of the dielectric boundary into a propagating wave, similar to the appearance of a propagating transmitted wave when a second prism is positioned in close proximity above the reflecting

interface in the case of frustrated TIR (5). Analogous to the classical 'double-prism' experiment, this propagating wave is directed into angles "forbidden" by Snell's law, and the phenomenon is hence termed "supercritical angle fluorescence" (SAF), **Fig. 1***B* (*bottom*) (2, 6, 7). Only fluorophores located very close to the dielectric boundary can emit SAF. The closer they are, the more of their emission is funneled into supercritical angles making SAF. Its near-exponential distance dependence makes SAF an absolute nanometric axial ruler insensitive to most aberration biases (6, 8-10). In turn, fluorophores distant from the interface cannot emit SAF at all, and their fluorescence is necessarily undercritical, **Fig. 1***C*. Thus, the selective detection of SAF vs. undercritical angle fluorescence (UAF) allows discriminating near-interface fluorophores against those located in the bulk (1).

II. SELECTIVE SAF DETECTION PERMITS THE ACQUISITION OF TIRF-LIKE IMAGES

Equally based on near-field/interface interactions, SAF and TIRF produce a similar optical sectioning. SAF collection in the solid-angle range above θ_c renders fluorescence *detection* surface-selective, much as supercritical fluorescence *excitation* confines TIRF. In TIRF, light propagating at high incidence angles produces a near-field close to an interface; in SAF, a near-field close to an interface generates high-angle emission. This is the optical reciprocity of TIRF and SAF. The similar axial confinement of both near-field techniques is illustrated in a cell-biological application by the pseudo-color overlay of TIRF and SAF images of green-fluorescent protein- (GFP-) expressing mitochondria in cultured cortical astrocytes taken with the same 1.46-NA objective, **Fig. 2***A* (*i*). TIRF images were acquired upon azimuthal beam spinning (11) at polar beam angles of $\theta = 64$, 68 and 70°, respectively, (*green*), and the SAF image (shown in *red* pseudocolor) was taken upon EPI-excitation ($\theta = 0$). For TIRF, the precise incidence angle θ determines the EW penetration depth $\delta(\theta)$ (although the 'true' excitation light distribution can be contaminated by unwanted stray light and long-range

excitation components (4, 12)). On the contrary, SAF exclusively depends on the axial fluorophore height h, so that the apparent overlap between TIRF and SAF images will generally vary with θ (13). Using Pearson's and Manders' coefficients (14) to quantify, respectively, the amount of co-variance of intensities and the overlap between the 'red' and 'green' pixels, we recognize that TIRF and SAF highlight similar structures ($R_{12} \approx 0.8$) but the fraction of pixels that overlap on the segmented SAF image with TIRF pixels (M_2) is steadily diminishing for higher θ, **Fig. 2***B*. This is plausible, because the TIRF excitation volume shrinks with increasing angle and becomes gradually more selective, eventually leading to a thinner optical section than SAF at very high beam angles, **Fig. 2***A* (*ii*).

However, grazing beam angles require positioning the focused laser spot very close to the objective's limiting θ_{NA}, which can produce stray excitation and degrade the excitation confinement and image contrast (12). In objective-type TIRF (15), several studies have documented the presence of an unwanted 5-10% of non-evanescent (long-range) excitation component that adds to the localized EW excitation (4, 12, 16, 17). Advantageously, TIRF excitation and SAF detection can be associated to relieve constraints on θ (13). Due to the combined excitation confinement and emission axial filtering, TIR-SAF images display a better optical sectioning than TIRF alone at the same θ, as result of suppressing contribution of the unwanted fluorescence from fluorophores located at deeper sample regions. Yet, as only the supercritical part of dipole radiation is being used, SAF images tend to be dimmer. Nevertheless, as a consequence of the efficient background suppression, they have a better signal-to-background ratio (SBR) than TIRF-alone images for the same excitation intensities as seen in a proof-of-concept experiment using tiny fluorescent microspheres as a fluorescence standard, **Fig. 2***C*.

Of course, SAF does not require TIRF excitation and SAF detection has been combined with many other excitation geometries, including epi-fluorescence, confocal-spot

187 excitation without (1, 18, 19) and with stimulated-emission depletion (STED) (20). A
188 growing body of spot-excitation and confocal SAF detection is devoted to supercritical
189 fluorescence correlation spectroscopy (FCS) (21-24). Finally, dipole-surface interactions and
190 supercritical-angle detection are not restricted to fluorescence: supercritical-angle
191 luminescence (SAL) detection (25) and supercritical-angle RAMAN (SAR) spectroscopy (26)
192 have been reported.
193

194 ## III. SELECTIVE DETECTION OF SUPER- CRITICAL EMISSION COMPONENTS

195 Whereas TIRF can be detected without specialized optics[2], **Fig. 3***A*, for SAF to be detected
196 one requires, (*i*), a *detection* NA>n_1 spanning supercritical angles and, (*ii*), a device for
197 angular emission filtering to reject the undercritical emission component that is dominated by
198 fluorophores in the bulk volume.

199 In early implementations, a low-NA central detection aperture and a surrounding high-
200 NA parabolic reflector were used to separate under- and supercritical emission components
201 (1, 18, 22, 34). When using the highly corrected imaging optics of a high-NA microscope
202 objective (2, 9, 10, 13), Abbe's sine condition provides an unambiguous relationship between
203 emission angles and radii in the objective's backfocal plane (BFP), providing a rationale for
204 FOURIER-PLANE FILTERING, $r\theta = f_{obj} \cdot n_2 \cdot \sin\theta$. Here, f_{obj} is the objective's focal length, f_{TL}/M,
205 i.e., the ratio of the focal length of the manufacturer tube lens and the objective transversal
206 magnification; see Ref. (27) for the subtleties for very-high NA objectives. One might
207 imagine to block UAF emission by simply placing an appropriately sized opaque disk in the
208 BFP. However, the BFP is located inside the objective lens, **Fig. 3***B*, so that a relay telescope
209 is needed to image the BFP into a CONJUGATE PLANE, **Fig. 3***C*. A caveat is that in either of the
210 geometries shown in panels *B* and *C* the effective detection aperture is reduced to a ring, so

[2] But TIRF needs a high-NA objective ref. (15) or, alternatively, the external prism ('Kretschmann') geometry for guiding light a supercritical angles to the interface.

that the lower-NA Fourier components are clipped, and only a tiny part of the objectives SPATIAL-FREQUENCY BANDWIDTH is used for image formation. However, while the wide-field image shows a degraded lateral resolution, the point-spread function is not significantly perturbed for confocal-spot detection (**Fig. 3***C*), where a lateral resolution of 226 ± 12 nm vs. 211± 9 nm has been reported in the SAF and confocal mode, respectively (18).

Thus, the SAF image obtained by just blocking out UAF has a lower resolution than the corresponding image taken at full aperture (28, 29). The precise positioning of an aperture stop is facilitated by a BERTRAND LENS, **Fig. 3***D*.

The spatial-resolution problem is elegantly avoided with *virtual SAF* (*v*SAF) detection (30). Here, an iris rather than a central disk is used as an aperture mask, and two images are acquired: one taken at the full NA, and the other with the effective detection aperture stopped down to NA' ≈ RI_{sample} ($\Leftrightarrow r_c = f_{obj} \cdot n_1$, where r_c is the critical radius marking the transition of UAF to SAF), **Fig. 3***E*. The first image contains both SAF and UAF emission components, the latter contains UAF only. Their difference image, *v*SAF = (SAF + UAF) – UAF, is a 'virtual' SAF image, equivalent to the one taken with the ring aperture and containing exclusively the fluorescence components emitted into supercritical angles. However, as two high-NA images are used for image formation, the lateral resolution is maintained. The downside of this image-subtraction approach is that by taking the (possibly small) difference between two (possibly bright) images, the shot noise of the difference on the resulting *v*SAF image can be much larger than the shot noise in straight SAF. If, in addition, the excitation is not TIRF, then a lot of useless fluorescence will be detected on the UAF image, which only increases the shot noise of the difference. In conclusion, the *v*SAF method has the advantage of preserving lateral resolution, but the disadvantage in photon statistics. Combined TIR-SAF partially circumvents this problem.

Alternative geometries do not use commercial objectives at all. As mentioned before, early SAF work used a custom high-NA parabolic ring-mirror (1) surrounding a central undercritical detection (and excitation) optical path instead of a high-NA objective. The same authors later presented a design that integrates separate high-NA and low-NA pathways within a custom objective lens (22), but this objective does not seem to be commercially available. Common to both geometries is that they use a point detection scheme and require sample scanning for SAF-image acquisition (18), similar to the formally equivalent (but rarely used) confocal spot-scanning TIRF geometry (31-33).

IV. SAF APPLICATIONS: MORE THAN SURFACE-SELECTIVE FLUORESCENCE

SAF can be used with simple aperture filtering as a surface-selective fluorescence technique and as an alternative to TIRF-based detection. However, when a BFP image is captured instead of (or in addition to) the sample plane image and the radiation pattern is analyzed, SAF can provide additional information (10). In the following, we present a non-exhaustive list of mostly recent applications and we discuss particularly, how SAF compares relative to various TIRF-based techniques, and we advocate quantitative uses of BFP-image information.

SAF applications with aperture filtering

Near-surface fluorescence. Surface-selective fluorescence detection is straightforward for non-imaging (sensing) applications (34, 35) or in confocal-spot scanning geometries (1, 18, 22), because no special requirements are imposed on the illumination optical path. This approach particularly interesting for background rejection either in large-area, multi-spot or multiplexed (multi-well) assays. Indeed SAF is increasingly being used for surface binding assays, the characterization of antibodies or sensitive toxin detection. In an attempt to scale up SAF sensing for even higher throughput, miniaturized parabolic optics have recently been integrated into the bottom of disposable plastic biochips (36) and polymer test tubes (37). A

truncated cone-shape geometry was shown to parallelize sensing in 256 spots on a microscope-slide sized biochip (38, 39). Yet, while useful for sensing, the large aberrations and missing central cone in these plastic "SAF chips" are prohibitive for imaging applications.

A short-sighted microscope. (a), implemented in a scanning geometry combining confocal-spot illumination with SAF collection on a point detector (18, 33) SAF is a powerful alternative to TIRF and related excitation-light confining 'highly inclined laminar optical sheet (HILO) techniques. However, while the lateral resolution and axial optical sectioning can of the order of, respectively, 220 and 100 nm (18) the stage-scanning requirement makes image acquisition too slow for imaging near-membrane dynamics in live cells.

(b), as a full-field technique either with a resolution-compromising aperture disk (29) or else in the resolution-preserving *v*SAF variant (13, 30, 40), SAF microscopy is a simple, cheap and less alignment-demanding whole-field alternative to TIRF. Additionally, no laser source is needed. Compatible with a host of illumination schemes and readily implemented on a standard inverted microscope, *v*SAF imaging is increasingly being used for imaging cell adhesion, cytoskeletal, vesicle- and membrane dynamics (see, however, the above comment on shot noise doubling). Also, we observed in vesicle-tracking experiments using FM1-43 labeling that SAF 'magnified' the relative importance of spurious, membrane-resident fluorophores that are more efficiently detected than their vesicular counterparts, only a few tens of nm deeper in the cell. Likewise, when used with epifluorescence excitation, the presence bulk fluorophores can dominate over the fainter SAF signal if $c_{\text{bulk}} >> c_{\text{membrane}}$. Thus, some prudence and careful controls are required for quantitative SAF uses and, depending on the specific fluorophore concentration profile, selective SAF detection can even reduce the signal-to-background ratio.

We advocated the use of SAF in conjunction with TIRF (13), particularly when using TIRF in the prismless, objective-type configuration. Here, SAF can help to remove impurities, imperfections and unknowns associated with the passage of the laser beam close to the limiting NA of the objective and those resulting from conjugate image planes inside the microscope body (4, 40). Also, contrary to the earlier discussed case of SAF with epifluorescence illumination, the combined excitation and emission optical sectioning result in a better surface-selectivity of fluorescence detection. Associated to the structured-illumination variant of TIRF, TIRF-SIM (41-45) SAF is expected to provide a true isotropic ~100-nm resolution.

Nanometer-axial fluorophore localization. The steep dependence of the SAF fraction of emitted fluorescence on the axial fluorophore distance h has prompted the use of SAF as a nanometric axial ruler with single-molecule sensitivity in a 150-200 nm range close to the interface (7, 10, 22). 3-D single-molecule localization with nm precision is offered through the combination of dSTORM and SAF (8). Hence, one prominent use of SAF is to remove the traditional imbalance of lateral and axial resolution in super-resolution microscopies by the SAF-based axial single-molecule localization.

We believe that this use of SAF as nanometric axial ruler is particularly powerful, as the SAF/UAF ratio (near-) exponentially depends on the axial fluorophore distance, but not on other (linear) factors, like the local illumination intensity, the fluorophore concentration or detection efficiency across the field-of-view that all cancel out during ratioing. Obvious applications include PALM, STORM, STED and TIRF-SIM microscopies with combined SAF detection.

Fluorescence correlation spectroscopy (FCS). The combined effect of confocal detection and SAF-mediated surface confinement can produce a tiny (attoliter, 10^{-18} l) detection volume. This feature has been used for ultrasensitive near-interface diffusion and concentration measurements via FCS (21, 24, 46). Simultaneous UAF and SAF detection permits the synchronous readout of bulk and near-surface mobility and concentration (47) and removes ambiguities resulting from axial motion in non-flat membrane stretches (23). Unlike TIR-FCS, SAF – and SAF-UAF-ratioing – has the advantage of being less sensitive to the excitation-light distribution and to define an observation volume through a unique fluorophore property, axial distance. A detailed treatment of the observation volume in a confocal-spot geometry is found in ref. (18).

SAF applications with BFP imaging and the analysis of the radiation pattern

SAF goes beyond axial optical sectioning when imaging the aperture (pupil) plane of a high-NA objective rather than its field (sample) plane, **Fig. 3***D*. The BFP image contains the fluorophore radiation pattern, which contains fluorophore information (see (10) for a recent overview). Depending on the exact geometry used, this information is derived either from a limited number of fluorophores in the confocal spot (33) or else integrated (averaged) over the entire field of view (40). In addition, how typical aberrations of high-NA objectives influence Fourier-plane images has been studied in detail (27).

Imaging molecular orientation. Albeit not called SAF at the time but "single-molecule detection with Fourier-plane image analysis", the dependence of the fluorophore radiation pattern on the orientation of the dipole axis relative to the optical axis has allowed studying molecular orientation (48), rotational dynamics (49, 50) and even nanometric axial movement in single-molecule (9) and single-nanoparticle detection assays (8), using a combination of

lateral single-molecule localization and SAF-based axial-distance assays. Backfocal imaging and spectroscopy have been applied not only to study angular emission patterns of fluorescent molecules, but also to investigate anisotropic Raman signals from molecules, elastic scattering, plasmonic scattering and non-linear scattering as well as secondary emission via optical antennas (see, e.g., (51) for a recent review and literature cited therein).

Variable-angle SAF spectroscopy. Surface-selective (immuno-) assays often require a wash step prior to read-out due to the otherwise overwhelming signal of the large number of unbound (bulk) fluorescent molecules that dominate over the signal from the molecules of interest, bound to the substrate. TIRF has been the method-of-choice for investigating the population of surface-bound fluorophores in isolation, and variable-angle scans (VA-TIRF) have allowed a 'tomographic' reconstruction of layer thickness, membrane topography, or cell adhesion from fluorophore distance (52-58).

SAF is an obvious alternative to VA-TIRF, but how the radiation pattern changes in the presence of surface-bound and bulk fluorophores had not been experimentally studied (59). The van Dorpe lab recently investigated how the collection angle influences the SAF surface sensitivity in the presence of bulk fluorophores. For this, two different fluorophores were used. One was bound to the surface and the other was dissolved in the bulk. Then, measuring the spectrum at discrete points in the back focal plane (BFP) by scanning a small optical fibre along the radial direction, the authors quantified the relative contribution of the two fluorophores using spectral imaging and linear unmixing. While the highest signal-to-noise ratio was observed in the region just above θ_c because of the higher signal intensity, the highest signal-to-bulk ratio was observed at much larger angles, at values above 68° for a glass/water interface. Thus, for experiments where bulk exclusion is important, increasing the NA enhances the surface sensitivity, however, restricting SAF detection to the outermost

high-NA rig comes at the cost of a decreased signal intensity. Obviously, this study inspires combining emission spectral imaging and spectral BFP image analysis for multi-color studies of the basal cell membrane or the nanoscale 3-D organization, e.g., for understanding the nano-architecture of cell adhesion sites and the peripheral multilayered cytoskeleton, which – at present - are typically being studied with variable-angle TIRF. Also, understanding the angular dependence on the sensitivity of a SAF biosensor will allow tuning the collection angles towards specific applications and contribute to designing smaller, more efficient devices.

Verification of high-NA objectives. When the RI of the fluorophore-embedding medium is known (as for air, water, or calibrated sucrose[3] or for a glycerol/water mix (60, 61)), the calibration of BFP radii via $r_c = f_{obj} \cdot n_1$ on a BFP image and application of Abbe's sine condition allows measuring the outer, bounding radius. This measurement directly provides the effective objective NA_{eff} via $r_{NA} = f_{obj} \cdot n_2 \cdot \sin\theta = f \cdot NA_{eff}$. SAF-based NA measurements are a simple and precise means to measure large NAs > $n_2 \cdot \sin\theta_c$ that are otherwise difficult to measure because of TIR (62). Using this strategy, we found important deviations between the true and specified NA for some objectives (Fig. S2 in Ref. (12)). A reduced effective NA is not only a relevant information prior to buying such expensive objective lenses (e.g., when upgrading from a 1.45 to a 1.49-NA lens), but it is also a factor causing stray excitation in TIRF experiments where a good optical sectioning, i.e., very high polar beam angles θ are sought for.

[3] Degrees Brix (°Bx) is the sugar content of an aqueous solution. One °Bx is 1 g of sucrose in 100 g of solution and represents the strength of the solution as mass %. The °Bx is traditionally used in the wine, sugar, carbonated beverage, fruit juice, maple yrup and honey industries, but the commercial availability of calibrated sucrose solution has also been exploited in science. See, e.g., Ref. (40).

382 *SAF refractometry.* Conversely, with NA_{eff} known, an interesting and new SAF application is
383 near-surface refractometry (40): as the transition of UAF to SAF depends on the sample RI n_1
384 (but not on n_2), the measurement of the "critical radius" $r_c = f_{obj} \cdot n_1$ on the BFP image allows
385 for a sensitive measurement of the *local* RI of the fluororphore-embedding medium. The
386 precision of this measurement depends on the quality of the fit of the BFP image (and hence
387 on the available signal, pixel size, and camera sensitivity), and typical RI values with ±0.001
388 error are being reached. This property has been used – together with diverse fluorophores that
389 we subcellularly targeted to different organelles – for intracellular RI-measurements (40). Of
390 note, even though wide-field SAF refractometry measures the *local* fluorophore environment,
391 it reports an *average* RI value, $<n_1>$, averaged over all SAF-emitting fluorophores in the
392 field-of-view. In an attempt to achieve spatially resolved RI measurements, a combination of
393 Bessel-beam-spot excitation with confocal intensity and simultaneous SAF-based RI
394 detection through the same high-NA objective has been reported in a recent communication
395 (33).
396
397 *Label-free RI-based SAF assay.* An interesting variant of this refractometric readout is SAF
398 detection from a fluorophore-coated glass microcapillary (63). Here, the analyte is non-
399 fluorescent and its presence sensed indirectly via the RI change. This change in the
400 fluorophore environment (detected as a shift in r_c and hence $<n_1>$) is induced by a medium
401 change or - as shown by the authors – by bacterial growth on the capillary bottom. In the
402 same manner, one can imagine to measure cell adhesion or confluency in unlabeled cell
403 cultures grown on a fluorophore-coated coverslip. In either case, the sensitivity of this label-
404 free fluorescent SAF assay will be limited by the fluorescence signal available after
405 prolongued use of the capillary sensor and by the timecourse of photobleaching of the

406 immobilized dye. Conceptually, the technique is reminiscent of nm-scale axial resolution with
407 non-radiative excitation, (64).
408
409 *Incidence-angle calibration in VA-TIRF.* BFP imaging of the SAF-ring has been used for
410 calibrating the polar beam angle θ in objective-type TIRF microscopy. Similar to the earlier
411 RI-measurement, the approach is based on a series of θ_c-measurements on BFP images using
412 a glass substrate topped with solvents having different RIs. In one study, a thin homogenous
413 layer of fluorophores in air was used to produce a SAF ring of known radius $r_c^{(air)} = f_{obj}$ that
414 was compared to the annular distribution of excitation light in azimuthal beam-spinning TIRF
415 with the fluorescence filter removed (65). Two follow-up studies used a similar strategy but
416 either with a thin layer of organic dye for TIRF-SIM calibration (45) or else with Qdots
417 embedded in PMMA for A-TIRFM (66). In the latter case, the fluorophore layer was topped
418 with solutions of different, known RI (previously measured with an Abbe refractometer) and
419 the laser spot (seen when the emission filter was taken out) steered to these known angles to
420 attain a more precise multi-angle calibration.
421
422 **V. WHAT'S NEXT?**
423 SAF, either used for surface-selective fluorescence detection or – combined with the analysis
424 of BFP images – for imaging the fluorophore radiation pattern, is an active and rapidly
425 expanding area of research. Beyond its early uses in spectroscopy, sensing and studies of
426 single-molecule mobility and rotation, SAF detection plays increasing roles in imaging
427 applications, either with wide-field detection or else as a confocal point-measurement
428 technique with sample scanning. Recent studies emphasized the quantitative analysis of BFP
429 images to extract various fluorophore properties, and ongoing work aims at the real-time
430 analysis of BFP images through rapid feature extraction. Future studies will likely combine an

analysis of the radiation pattern with fluorescence-intensity, life-time or anisotropy-based contrast, marking the arrival of SAF-based multi-modal microscopies.

Given that these applications all rely on BFP image analysis we expect deep-learning to have an impact similar to other fields of microscopic image analysis. Artificial intelligence (AI) based BFP image analysis will boost information-extraction from the narrow high-intensity ring characteristic for SAF. Fast feature recognition – particularly when multiple emitters or multi-color emitters are present - and adaptive aperture filtering are only two aspects that will benefit from AI, in a manner similar to exploiting the chromatic dependence of PSF shapes from different emitters imaged on a grayscale camera (67).

The relative ease of use, reduced complexity and (compared to TIRF) low price of instrumentation required for *v*SAF is most likely to increase its dissemination of the for routine biological microscopy. A '*v*SAF-module' that can be fitted between the microscope exit port and an existing EMCCD or sCMOS camera is now commercially available (by the French start-up Abbelight – non-related to the authors), and makes the technique accessible for non-expert users.

Finally, in as much as SAF does not depend on how fluorescence was excited but represents an intrinsic fluorophore property depending solely on its distance from the interface, we foresee a growing use of SAF in microscope calibration and standardization applications (4).

List of abbreviations

AI	-	artificial intelligence
BFP	-	back-focal plane
EMCCD	-	electron-multiplying charge-coupled device
EW	-	evanescent wave

457	FCS	-	fluorescence correlation spectroscopy
458	FWHM	-	full width at half maximum
459	HILO	-	highly inclined laminar optical (sheet)
460	NA	-	numerical aperture
461	PCC	-	Pearson's correlation coefficient
462	PMMA	-	poly(methyl methacrylate)
463	PSF	-	point spread function
464	RI	-	refractive index
465	SAF	-	supercritical angle fluorescence
466	SBR	-	signal-to-background ratio
467	sCMOS	-	scientific complementary metal oxide sensor
468	STED	-	stimulated emission depletion microscopy
469	TIR(F)	-	total internal reflection (fluorescence)
470	UAF	-	under-critical angle fluorescence

471

472

473 **Glossary**

474 APERTURE (OR BACKFOCAL) PLANE – in a multi-lens system, a plane conjugate to the aperture,
475 in a light microscope, the set of conjugate aperture planes comprises the exit pupil, objective
476 back-focal plane, condenser front focal plane and the lamp filament. (see also field plane for
477 the other set of conjugate planes including the sample plane and detector).
478 BERTRAND LENS – an optical device used in aligning the various optical components of a light
479 microscope. It allows observation of the back focal plane of the objective lens and its
480 conjugated focal planes.
481
482 FOURIER FILTERING – refers to modulating or clipping in frequency space; in SAF, it refers to
483 shaping the SPATIAL FREQUENCY BANDWIDTH of the microscope by selectively attenuating,

484 blocking or enhancing certain segments of the (conjugate) back-focal plane by an aperture
485 mask.

486 NUMERICAL APERTURE (NA = $n \cdot \sin\theta_{NA}$) – Magnitude related to the maximal angle of
487 collection or excitation of an optical element.

488 (OBJECTIVE) BACK-FOCAL PLANE (BFP) – Effective rear focal plane of the assembly of lens
489 composing the objective. For most objective lenses, it is located inside the objective and
490 hence only accessible by generating an intermediate image in a conjugate plane.

491 OPTICAL RECIPROCITY – (for all practical grounds here) principle that describes how a ray of
492 light and its reverse follow the same optical path.

493 RAMAN (SCATTERING) – Inelastic scattering of a photon when it encounters matter.

494 SNELL'S LAW – A law from geometrical optics that describes how a ray of light is reflected
495 and/or transmitted when it encounters an interface between two different refractive-index
496 media, $n_i \cdot \sin\theta_i = const.$

497 SPATIAL-FRENQUENCY BANDWIDTH - Range of frequencies that is transmitted by the system.
498 In an optical (or imaging) system this bandwidth is inversely related to the spatial optical
499 resolution. See also Object transfer function and Point Spread Function.

500 SUPERCRITICAL ANGLE FLUORESCENCE (SAF) – Fluorescence that propagates trough a higher-
501 index medium (compared to the emission medium) at 'forbidden' angles higher than the
502 critical angle.

503 TOTAL INTERNAL REFLECTION (TIR) – Complete bouncing back of a beam from a transparent
504 interface (i.e., no transmitted light) that can occur when a light impinges at an interface from
505 the higher- (n_2) to the lower-refractive index side (n_1), at an angle larger than a certain critical
506 angle, $\theta_c = \text{asin}(n_2/n_1)$.

507

508 ACKNOWLEDGEMENTS

This study was supported by a *Chaire d'Excellence Junior University Sorbonne Paris Cité*, USPC (to MB), the Israeli Science Foundation (ISF-NSFC 2525/17, to AS), the European Union (H2020 Eureka! Eurostars NANOSCALE (to MO and AS). Our collaborative research on TIRF and SAF was further financed by a French-Israeli ImagiNano CNRS-LIA grant (to AS & MO), the *Agence Nationale de la Recherche* (ANR-10-INSB-04-01, *grands investissements* FranceBioImaging, FBI, to MO), the Université Paris Descartes (invited professorship during the academic year 2017-18, to AS) and the French *Ministère des Affaires Etrangères* (Chateaubriand Senior Fellowship to AS). The authors thank Dana Khanafer for help with Fig. 2*C*. The Oheim lab is a member of the C'nano IdF and *Ecole de Neurosciences de Paris* (ENP) excellence clusters for nanobiotechnology and neurosciences, respectively.

Author contributions

All authors contributed to experiments. The manuscript was written by MO with contributions of all authors. All authors have given their approval to the final version of the manuscript.

Notes

The authors declare no competing financial interest.

REFERENCES

1. Ruckstuhl, T., J. Enderlein, S. Jung, and S. Seeger. 2000. Forbidden light detection from single molecules. Anal. Chem. 72:2117-2123.
2. Axelrod, D. 2013. Evanescent excitation and emission in fluorescence microscopy. Biophys. J. 104(7):1401-1409.
3. Oheim, M. 2016. TIRF (Total Internal Reflection Fluorescence). eLS. John Wiley & Sons, Ltd.
4. Oheim, M., A. Salomon, A. Weissman, M. Brunstein, and U. Becherer. 2019. Calibrating evanescent-wave penetration depths for biological TIRF microscopy. Biophys. J. 117(5):795-809.
5. Harrick, N., and K. Beckmann. 1974. Internal reflection spectroscopy. Characterization of Solid Surfaces. Springer, pp. 215-245.

6. Hellen, E. H., and D. Axelrod. 1987. Fluorescence emission at dielectric and metal-film interfaces. JOSA B 4(3):337-350.
7. Axelrod, D. 2012. Fluorescence excitation and imaging of single molecules near dielectric-coated and bare surfaces: a theoretical study. J. Microsc. 247(2):147-160.
8. Bon, P., N. Bourg, S. Lécart, S. Monneret, E. Fort, J. Wenger, and S. Lévêque-Fort. 2015. Three-dimensional nanometre localization of nanoparticles to enhance super-resolution microscopy. Nat. Commun. 6:7764.
9. Bourg, N., C. Mayet, G. Dupuis, T. Barroca, P. Bon, S. Lécart, E. Fort, and S. Lévêque-Fort. 2015. Direct optical nanoscopy with axially localized detection. Nat. Photonics 9(9):587.
10. Brunstein, M., A. Salomon, and M. Oheim. 2018. Decoding the information contained in fluorophore radiation patterns. ACS Nano 12(12):11725-11730.
11. van't Hoff, M., V. de Sars, and M. Oheim. 2008. A programmable light engine for quantitative single molecule TIRF and HILO imaging. Opt. Express 16(22):18495-18504.
12. Brunstein, M., M. Teremetz, K. Hérault, C. Tourain, and M. Oheim. 2014. Eliminating unwanted far-field excitation in objective-type TIRF. Part I. identifying sources of nonevanescent excitation light. Biophys. J. 106(5):1020-1032.
13. Brunstein, M., K. Hérault, and M. Oheim. 2014. Eliminating unwanted far-field excitation in objective-type TIRF. Part II. combined evanescent-wave excitation and supercritical-angle fluorescence detection improves optical sectioning. Biophys. J. 106(5):1044-1056.
14. Manders, E., F. Verbeek, and J. Aten. 1993. Measurement of co-localization of objects in dual-colour confocal images. Journal of microscopy 169(3):375-382.
15. Stout, A. L., and D. Axelrod. 1989. Evanescent field excitation of fluorescence by epi-illumination microscopy. Applied optics 28(24):5237-5242.
16. Mattheyses, A. L., and D. Axelrod. 2006. Direct measurement of the evanescent field profile produced by objective-based total internal reflection fluorescence. J. Biomed. Opt. 11(1):014006-014006-014007.
17. Niederauer, C., P. Blumhardt, J. Mücksch, M. Heymann, A. Lambacher, and P. Schwille. 2018. Direct characterization of the evanescent field in objective-type total internal reflection fluorescence microscopy. Opt. Express 26(16):20492-20506.
18. Ruckstuhl, T., and D. Verdes. 2004. Supercritical angle fluorescence (SAF) Microscopy. Opt. Express 12(18):4246-4254.
19. Sivankutty, S., T. Barroca, C. Mayet, G. Dupuis, E. Fort, and S. Lévêque-Fort. 2014. Confocal supercritical angle microscopy for cell membrane imaging. Opt. Lett. 39(3):555-558.
20. Sivankutty, S., I. C. Hernández, N. Bourg, G. Dupuis, and S. Lévêque-Fort. 2019. Supercritical angle fluorescence for enhanced axial sectioning in STED microscopy. Methods.
21. Ries, J., T. Ruckstuhl, D. Verdes, and P. Schwille. 2008. Supercritical angle fluorescence correlation spectroscopy. Biophys. J. 94(1):221-229.
22. Ruckstuhl, T., D. Verdes, C. M. Winterflood, and S. Seeger. 2011. Simultaneous near-field and far-field fluorescence microscopy of single molecules. Opt. Express 19(7):6836-6844.
23. Winterflood, C. M., T. Ruckstuhl, N. P. Reynolds, and S. Seeger. 2012. Tackling Sample-Related Artifacts in Membrane FCS Using Parallel SAF and UAF Detection. ChemPhysChem 13(16):3655-3660.
24. Ma, Y., A. Benda, P. R. Nicovich, and K. Gaus. 2016. Measuring membrane association and protein diffusion within membranes with supercritical angle fluorescence microscopy. Biomedical optics express 7(4):1561-1576.
25. Blue, R., N. Kent, L. Polerecky, H. McEvoy, D. Gray, and B. MacCraith. 2005. Platform for enhanced detection efficiency in luminescence-based sensors. Elec. Lett. 41(12):682-684.
26. Serrano, D., and S. Seeger. 2017. Supercritical angle Raman microscopy: a surface-sensitive nanoscale technique without field enhancement. Light: Sci. & Appl. 6(10):e17066.
27. Kurvits, J. A., M. Jiang, and R. Zia. 2015. Comparative analysis of imaging configurations and objectives for Fourier microscopy. JOSA A 32(11):2082-2092.
28. Enderlein, J., I. Gregor, and T. Ruckstuhl. 2011. Imaging properties of supercritical angle fluorescence optics. Opt. Express 19(9):8011-8018.
29. Barroca, T., K. Balaa, J. Delahaye, S. Lévêque-Fort, and E. Fort. 2011. Full-field supercritical angle fluorescence microscopy for live cell imaging. Optics letters 36(16):3051-3053.

30. Barroca, T., K. Balaa, S. Lévêque-Fort, and E. Fort. 2012. Full-field near-field optical microscope for cell imaging. Phys. Rev. Lett. 108(21):218101.
31. Chon, J. W., and M. Gu. 2004. Scanning total internal reflection fluorescence microscopy under one-photon and two-photon excitation: image formation. Appl. Opt. 43(5):1063-1071.
32. Terakado, G., K. Watanabe, and H. Kano. 2009. Scanning confocal total internal reflection fluorescence microscopy by using radial polarization in the illumination system. Appl. Opt. 48(6):1114-1118.
33. Szederkenyi, K., B. Lagarde, M. Brunstein, M. Guillon, C. Yip, and M. Oheim. 2020. Investigating Polarisation Effects in a Confocal Total Internal Reflection-Supercritical Angle Fluorescence (TIR-SAF) Geometry with Sample Scanning Biophys. J. abstract.
34. Ruckstuhl, T., M. Rankl, and S. Seeger. 2003. Highly sensitive biosensing using a supercritical angle fluorescence (SAF) instrument. Biosens. Bioelec. 18(9):1193-1199.
35. Kurzbuch, D., J. Bakker, J. Melin, C. Jönsson, T. Ruckstuhl, and B. MacCraith. 2009. A biochip reader using super critical angle fluorescence. Sens. Actuat. B: Chemical 137(1):1-6.
36. Hill, D., B. McDonnell, S. Hearty, L. Basabe-Desmonts, R. Blue, M. Trnavsky, C. McAtamney, R. O'Kennedy, and B. D. MacCraith. 2011. Novel disposable biochip platform employing supercritical angle fluorescence for enhanced fluorescence collection. Biomed. microdev. 13(4):759-767.
37. Ruckstuhl, T., C. M. Winterflood, and S. Seeger. 2011. Supercritical angle fluorescence immunoassay platform. Anal. Chem. 83(6):2345-2350.
38. Hung, T. Q., Y. Sun, C. E. Poulsen, T. Linh-Quyen, W. H. Chin, D. D. Bang, and A. Wolff. 2015. Miniaturization of a micro-optics array for highly sensitive and parallel detection on an injection moulded lab-on-a-chip. Lab on a Chip 15(11):2445-2451.
39. Nguyen, T., T. A. Ngo, D. D. Bang, and A. Wolff. 2019. Optimising the supercritical angle fluorescence structures in polymer microfluidic biochips for highly sensitive pathogen detection: a case study on Escherichia coli. Lab on a Chip 19(22):3825-3833.
40. Brunstein, M., L. Roy, and M. Oheim. 2017. Near-membrane refractometry using supercritical angle fluorescence. Biophys. J. 112(9):1940-1948.
41. Fiolka, R., M. Beck, and A. Stemmer. 2008. Structured illumination in total internal reflection fluorescence microscopy using a spatial light modulator. Opt. Lett. 33(14):1629-1631.
42. Kner, P., B. B. Chhun, E. R. Griffis, L. Winoto, and M. G. Gustafsson. 2009. Super-resolution video microscopy of live cells by structured illumination. Nat. Methods 6(5):339.
43. Brunstein, M., K. Wicker, K. Hérault, R. Heintzmann, and M. Oheim. 2013. Full-field dual-color 100-nm super-resolution imaging reveals organization and dynamics of mitochondrial and ER networks. Opt. Express 21(22):26162-26173.
44. Young, L. J., F. Ströhl, and C. F. Kaminski. 2016. A guide to structured illumination TIRF microscopy at high speed with multiple colors. JoVE (J. Vis. Exp.)(111):e53988.
45. Chen, Y., R. Cao, W. Liu, D. Zhu, Z. Zhang, C. Kuang, and X. Liu. 2018. Widefield and total internal reflection fluorescent structured illumination microscopy with scanning galvo mirrors. J. Biomed. Opt. 23(4):046007.
46. Ries, J., and P. Schwille. 2008. New concepts for fluorescence correlation spectroscopy on membranes. Phys. Chem. Chem. Phys. 10(24):3487-3497.
47. Winterflood, C. M., and S. Seeger. 2016. Simultaneous surface-near and solution fluorescence correlation spectroscopy. J. Fluoresc. 26(3):753-756.
48. Mattheyses, A. L., and D. Axelrod. 2005. Fluorescence emission patterns near glass and metal-coated surfaces investigated with back focal plane imaging. J. Biomed. Opt. 10(5):054007.
49. Lieb, M. A., J. M. Zavislan, and L. Novotny. 2004. Single-molecule orientations determined by direct emission pattern imaging. JOSA B 21(6):1210-1215.
50. Backer, A. S., and W. Moerner. 2014. Extending single-molecule microscopy using optical Fourier processing. J. Phys. Chem. B 118(28):8313-8329.
51. Vasista, A. B., D. K. Sharma, and G. P. Kumar. 2018. Fourier plane optical microscopy and spectroscopy. digital Encyclopedia of Applied Physics:1-14.

52. Reichert, W., P. Suci, J. Ives, and J. Andrade. 1987. Evanescent detection of adsorbed protein concentration-distance profiles: fit of simple models to variable-angle total internal reflection fluorescence data. Appl. Spectrosc. 41(3):503-508.
53. Burmeister, J. S., G. A. Truskey, and W. M. Reichert. 1994. Quantitative analysis of variable-angle total internal reflection fluorescence microscopy (VA-TIRFM) of cell/substrate contacts. J. Microsc. 173(1):39-51.
54. Oheim, M., D. Loerke, B. Preitz, and W. Stuhmer. 1999. Simple optical configuration for depth-resolved imaging using variable-angle evanescent-wave microscopy. In Optical biopsies and microscopic techniques III. SPIE, editor. Proc. SPIE - International Society for Optics and Photonics. 131-140.
55. Loerke, D., B. Preitz, W. Stuhmer, and M. Oheim. 2000. Super-resolution measurements with evanescent-wave fluorescence-excitation using variable beam incidence. J. Biomed. Opt. 5(1):23-31.
56. Stock, K., R. Sailer, W. S. Strauss, M. Lyttek, R. Steiner, and H. Schneckenburger. 2003. Variable-angle total internal reflection fluorescence microscopy (VA-TIRFM): realization and application of a compact illumination device. J. Microsc. 211(1):19-29.
57. Dos Santos, M. C., R. Déturche, C. Vézy, and R. Jaffiol. 2014. Axial nanoscale localization by normalized total internal reflection fluorescence microscopy. Opt. Lett. 39(4):869-872.
58. Dos Santos, M. C., R. Déturche, C. Vézy, and R. Jaffiol. 2016. Topography of Cells Revealed by Variable-Angle Total Internal Reflection Fluorescence Microscopy. Biophys. J. 111(6):1316-1327.
59. James Shirley, F., P. Neutens, R. Vos, M. Mahmud-Ul-Hasan, L. Lagae, N. Verellen, and P. Van Dorpe. 2018. Supercritical Angle Fluorescence Characterization Using Spatially Resolved Fourier Plane Spectroscopy. Anal. Chem. 90(7):4263-4267.
60. Hoyt, L. 1934. New table of the refractive index of pure glycerol at 20 C. Ind. Engin. Chem. 26(3):329-332.
61. Vural, U. S., V. Muradoglu, and S. Vural. 2011. Excess molar volumes, and refractive index of binary mixtures of glycerol+ methanol and glycerol+ water at 298.15 K and 303.15 K. Bull. Chem. Soc. Ethiopia 25(1):111-118.
62. Dai, L., I. Gregor, I. von der Hocht, T. Ruckstuhl, and J. Enderlein. 2005. Measuring large numerical apertures by imaging the angular distribution of radiation of fluorescing molecules. Opt. Express 13(23):9409-9414.
63. Ferdman, B., L. E. Weiss, O. Alalouf, Y. Haimovich, and Y. Shechtman. 2018. Ultrasensitive Refractometry via Supercritical Angle Fluorescence. ACS nano 12(12):11892-11898.
64. Riachy, L., D. El Arawi, R. Jaffiol, and C. Vézy. 2018. Non Radiative Excitation Fluorescence Microscopy: A New Method for Studying Membrane Adhesion at the Nanoscale. Biophys. J. 114(3):164a-165a.
65. Soubies, E., S. Schaub, A. Radwanska, E. Van Obberghen-Schilling, L. Blanc-Féraud, and G. Aubert. 2016. A framework for multi-angle TIRF microscope calibration. In 2016 IEEE 13th International Symposium on Biomedical Imaging (ISBI). IEEE, editor. IEEE, Prague, Czech Republic. 668-671.
66. El Arawi, D., M. C. Dos Santos, C. Vézy, and R. Jaffiol. 2019. Incidence angle calibration for prismless total internal reflection fluorescence microscopy. Opt. Lett. 44(7):1710-1713.
67. Michaeli, T., and Y. Shechtman. 2018. Multicolor localization microscopy by deep learning. arXiv preprint arXiv:1807.01637.

FIGURE LEGENDS

FIGURE 1. *Evanescence in excitation and emission.* (A), *top*, we assume for the purpose of this paper a planar dielectric interface separating two homogenous media having different refractive indices (RIs), $n_2 > n_1$. Snell's law $n_1 \cdot sin(\theta_1) = n_2 \cdot \sin(\theta_1)$ governs the angles of refraction at a dielectric interface. For a glass/water interface ($n_2 > n_1$), light impinging at the interface from the side of the denser medium 2 is totally reflected beyond a critical angle of incidence, $\theta_c = \text{asin}(n_2/n_1)$. Total reflection creates an inhomogeneous, propagating evanescent wave (EW) right above the dielectric boundary in medium 1, *bottom*. **S** is the Pointing vector, indicating the direction of energy flux. (B), fluorescence emission of near-interface dipoles. Far-field emission pattern from a radiating dipole located far from the interface (fluorophore height $h >> \lambda$) showing the familiar "laying-8" pattern. Molecular rotation (arrow) in solution often results in an isotropic fluorescence emission (dashed circle). The collected fraction of fluorescence hence depends on the solid angle captured by the NUMERICAL APERTURE (NA) of the objective. On the contrary, for $h \lesssim \lambda$, fluorescent specimen does not emit fluorescence isotropically, but approximately 2/3 of the fluorescence is emitted into the higher-index medium. Of this emission, the main part is directed to solid angles above the critical angle. On the contrary, already for $h = \lambda/2$, fluorescence above the critical angle is decreased dramatically. Hence, like TIRF, supercritical angle fluorescence (SAF) is suited to discriminate between molecules at or near to surfaces and other fluorophores in the bulk. (C), provided the detection NA of the collection optics is sufficiently large (NA > n_1), supercritical (SAF) and undercritical fluorescence emission components (UAF) can be collected simultaneously and separated in the in the objective backfocal plane (BFP). SAF and UAF can be distinguished as they travel at different NAs (i.e., radii in the BFP), which can be used for aperture filtering (see main text).

FIGURE 2. *SAF detection of TIRF-like images and combined TIR-SAF acquisition with improved contrast.* (A), TIRF (*green*) and (epi-excited) SAF (*red*) images of EGFP-expressing mitochondria in a cultured cortical astrocyte. For TIRF the polar beam angle was $\theta = 64$, 68 and 70° as indicated. (B), Evolution of Manders' co-localization coefficient M_1 for SAF (image 1, *red*) and of Pearsons correlation coefficient (PCC, *black*, see Ref. (14)). TIRF and SAF highlight similar structures ($\langle R_{12} \rangle = 0.79 \pm 0.01$). Unlike PCC, M_1 measures the amount of TIRF pixels coinciding with SAF pixels following thresholding of each channel. TIRF and SAF images are similar for intermediate beam angles (lower EW penetration depths), before TIRF becomes more discriminative at very high θ. However, this object-based analysis obscures the gain in sensitivity by SAF. (C), Contrast of TIRF-alone and combined TIR-SAF images. Images of yellow-green emitting 93-nm diameter beads upon 488-nm excitation and the FWHM and Michelson contrast ('visibility') calculated as $C_M = (I_{max} - I_{min})/(I_{max} + I_{min})$. Pixel size was 103 nm, $t_{exp} = 50$ ms. Symbols are measured intensity mean ± *SD* from

four independent measurements. Through lines are weighted Gaussian fits. SBR was 4.92 ± 0.16, C_M = 0.71 and FWHM = 293 ± 2 nm for TIRF alone; vs. SBR = 14.4 ± 1.1, C_M = 0.88, FWHM = 311 ± 1 nm for TIR-SAF. Thus, while no large difference was observed between FWHMs, the combined optical sectioning of TIRF excitation and SAF detection almost tripled contrast (×2.93).

FIGURE 3. *Microscope geometries for TIRF and SAF detection.* (A), typical optical layout for prismless ('through-the-objective') type evanescent-wave excitation. In the simplest case, an expanded laser beam is focused in an eccentric position in the BFP of a high-NA objective. ex – excitation light, obj – objective lens, dic – dichroic mirror, TL – tube lens, sCMOS – scientific complementrary metal-oxyde sensor. (B), hypothetical selective SAF detection with an opaque aperture mask in the objective BFP. (C), pracitical implementation of SAF detection with an aperture mask placed in a conjugate aperture plane, produced by a '4*f*' relay telescope. Like the arrangement shown in panel C, this scheme results in a resolution loss due to the ring aperture and clipping of central rays. (D), insertion fo a Bertrand lens (BL) allows BFP (or "Fourier-plane") imaging. (E), virtual SAF, *v*SAF configuaration, in which an iris stop is used instead of an opaque disk and the SAF image is calculated from the difference of two images taken with the iris open and stopped down to $NA' = n_1$, respectively. *Inset* images at the bottom represent the fluorescence radiation patterns observed by imaging the BFP of the objective in the various configurations.

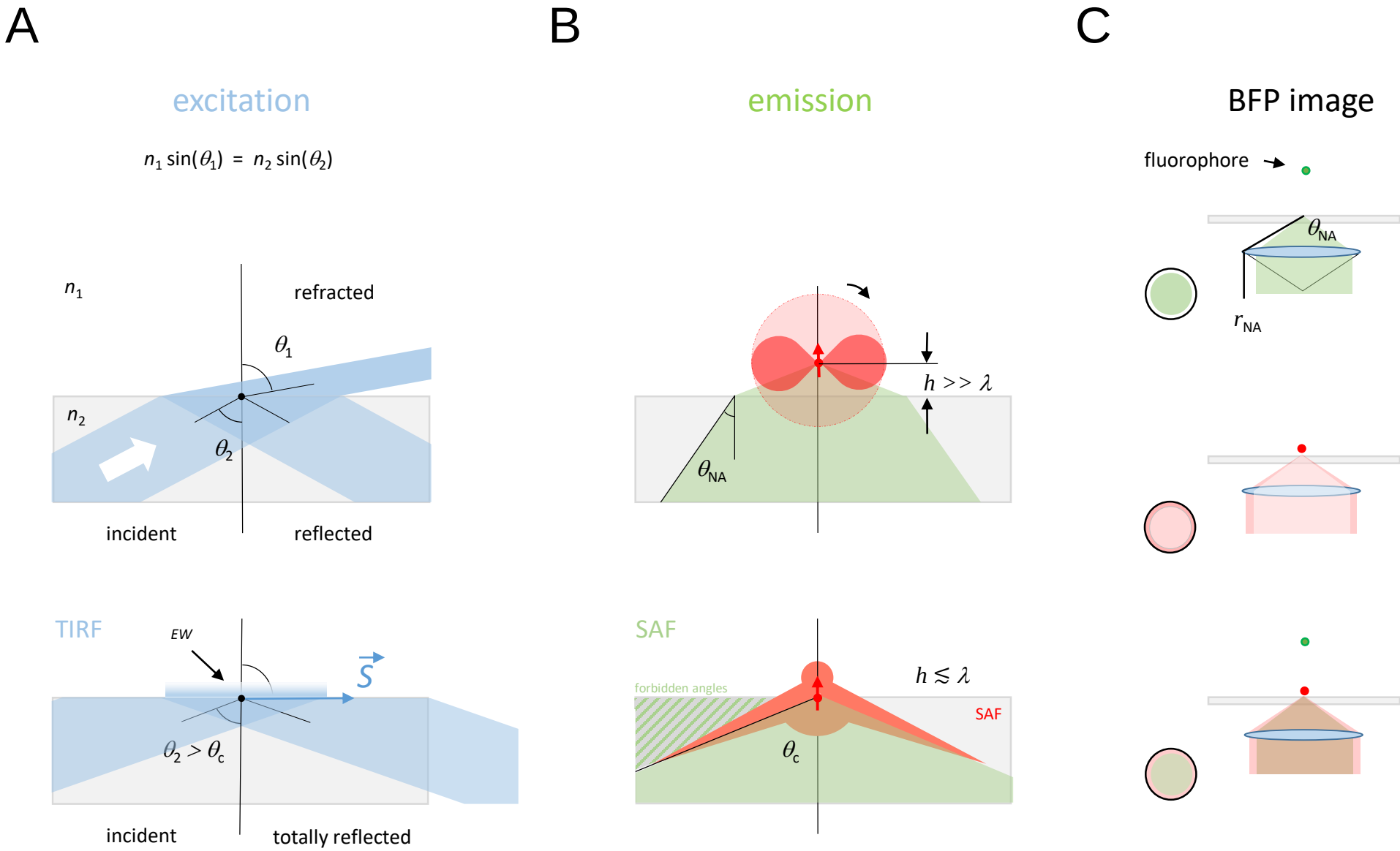

Oheim *et al.* **Fig. 1**

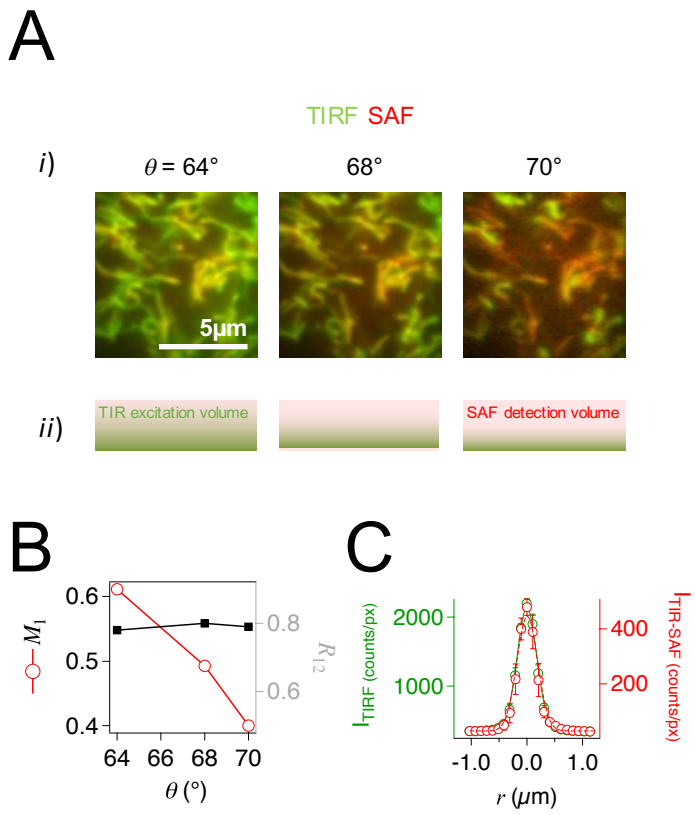

Oheim *et al.* **Fig. 2**

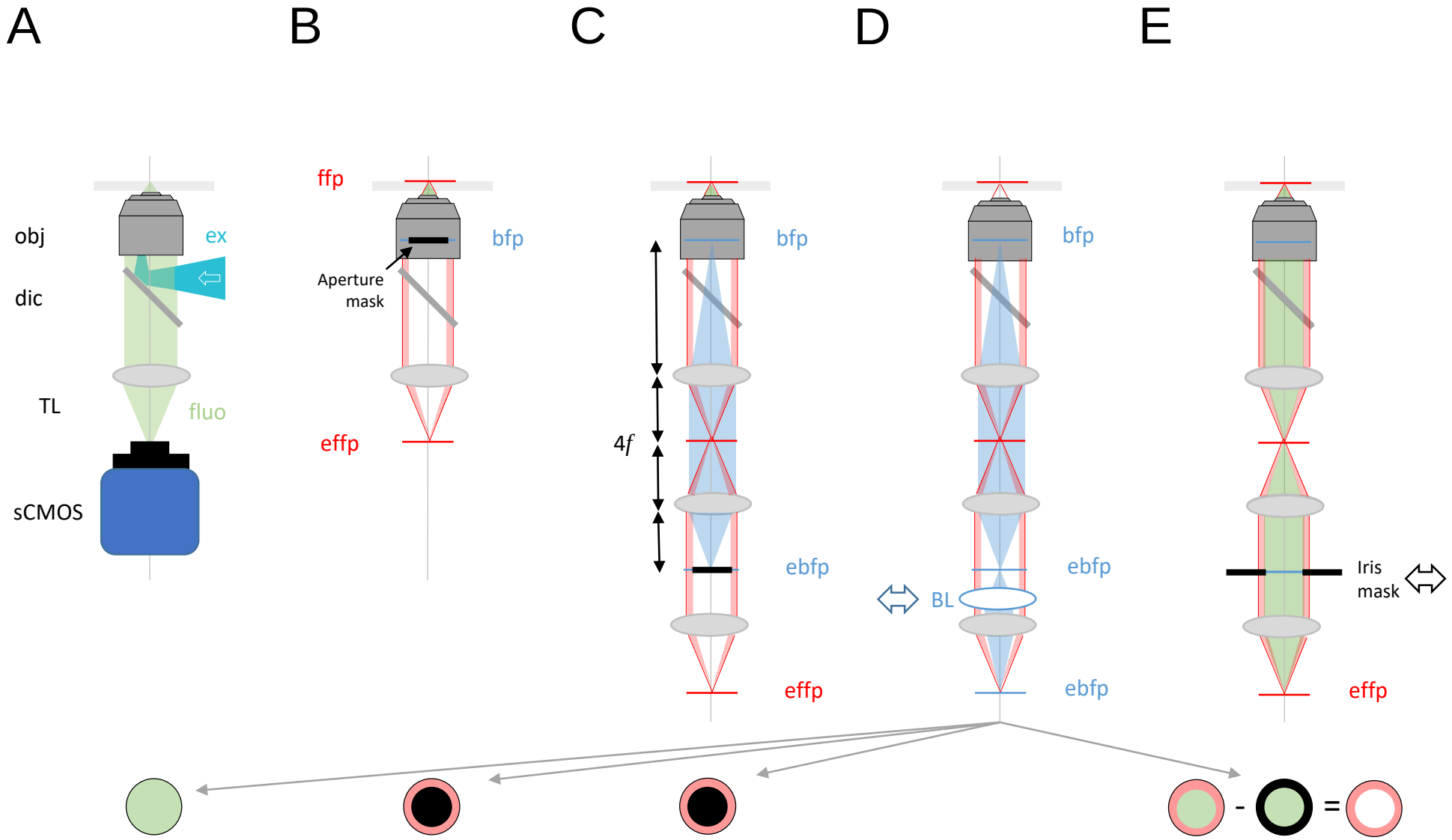

Oheim *et al.* **Fig. 3**